

# Future proofing network encryption technology (and securing critical infrastructure data) with continuous-variable quantum key distribution

Nitin Jain,<sup>1</sup> Hou-Man Chin,<sup>1</sup> Dev Null,<sup>1</sup> Adnan A.E. Hajomer,<sup>1</sup> Henrik Larfort,<sup>2</sup>  
Naja Lautrup Nysom,<sup>1</sup> Erik Bidstrup,<sup>3</sup> Ulrik L. Andersen,<sup>1</sup> and Tobias Gehring<sup>1,\*</sup>

<sup>1</sup>*Department of Physics, Technical University of Denmark, 2800 Kongens Lyngby, Denmark*

<sup>2</sup>*Energinet, Tonne Kjærsvej 65, 7000 Fredericia, Denmark*

<sup>3</sup>*Centre for Cyber Security (CFCS), Kastellet 30, 2100 Copenhagen, Denmark*

We demonstrate the establishment of quantum-secure data transfer links at two locations in Denmark: on the campus of Technical University of Denmark (DTU) in Lyngby and between two power grid nodes owned and operated by Energinet in Odense. Four different channels were investigated, one being a purely underground fiber and the other three being combinations of underground fibers and optical ground wires (OPGWs). Coherent ‘quantum’ states at 1550 nm, prepared and measured using a semi-autonomous continuous-variable quantum key distribution (CVQKD) prototype, were multiplexed in wavelength with ‘classical’ 100G encrypted data traffic from a pair of commercial layer-2 network encryption devices operating at around 1300 nm. At DTU, we estimate average secret key rates in the asymptotic limit of 1.12 Mbps (channel loss of 5.5 dB at 1550 nm) while at Energinet, the figures corresponding to the three channels (with losses of 4.1, 6.7, and 8.9 dB) are 2.05, 0.90, and 0.23 Mbps, respectively. The demonstration showcases that QKD can serve as an additional layer to protect sensitive network traffic propagating on insecure channels.

## I. INTRODUCTION

The explosion in the data traffic volumes in the last few years, driven by rapid growth of data centers and cloud service providers, poses significant security challenges. This is due to the nature of the data involved, which ranges from critical national infrastructure and user identities to financial secrets such as intellectual property, all of which are at risk. In particular, the energy infrastructure has been increasingly targeted, as evidenced by incidents such as the breach at a nuclear power plant in India [1], the Colonial Pipeline ransomware case in USA [2], and most recently, the coordinated hacking of 22 different energy companies in Denmark [3]. These events highlight a worrisome trend of increasing frequency, sophistication, and involvement of nation-states in cyberattacks.

While implementing good practices, such as timely application of patches and measures to prevent exploitation of vulnerabilities can never be underscored more, cryptographic solutions such as encryption add a protective layer on the sensitive data to foil adversaries. In the industrial context, a typical approach involves the use of hardware encryption devices, also known as network encryptors or Ethernet encryptors [4]. The devices, employing symmetric cryptographic algorithms such as advanced encryption standard (AES), operate in pairs, utilizing the same sequence of pre-configured keys for encryption and decryption of data.

A natural method to distribute random symmetric keys across an insecure communication channel is provided by quantum key distribution (QKD) [5–7]. In QKD, two users, Alice and Bob, can share quantum correlations through the exchange of quantum-optical sig-

nals, while ensuring that an eavesdropper, Eve, cannot intercept these correlations without getting disclosed. This is because any attempt by Eve to eavesdrop introduces noise and/or loss that Alice and Bob can quantitatively estimate, assuming pre-calibrated devices.

For QKD to become a practical cryptographic technology, one major challenge is its integration into existing optical communication infrastructure. The increased loss and noise from the telecommunication equipment, often attributed to the actions of an eavesdropper, adversely affects the key generation. Nonetheless, the QKD community has made significant progress, and several studies and field trials over the last decade have experimentally verified the feasibility of multiplexing QKD signals with classical data traffic without substantial performance degradation for either [8–12].

In this work, we showcase an example of quantum-classical integration for securing data in transit using QKD and network encryption. A semi-autonomous, telecom-rack mountable continuous-variable (CV) QKD system [13–15], operating at 1550 nm, produced a secret keystream for a pair of layer 2 network encryptors [16], communicating simultaneously over the same channel using 100G optical transceivers at  $1300 \pm 10$  nm.

Experiments were conducted at two locations in Denmark using four different combinations of underground and aerial fibers acting as the channel for the propagation of the C-band quantum states and the O-band optical signals. Off-the-shelf coarse wavelength division multiplexers (CWDMs) were used for their union and separation. The experimental scheme, illustrated in Figure 1, involved initial tests on a loopback single-mode fiber (SMF) under the Lyngby campus of Technical University of Denmark (DTU) to optimize the system operation, followed by temporary installation and testing at the premises of Energinet in Odense. Here, we explored three different loopback topologies using optical ground

\* Corresponding author: tobias.gehring@fysik.dtu.dk

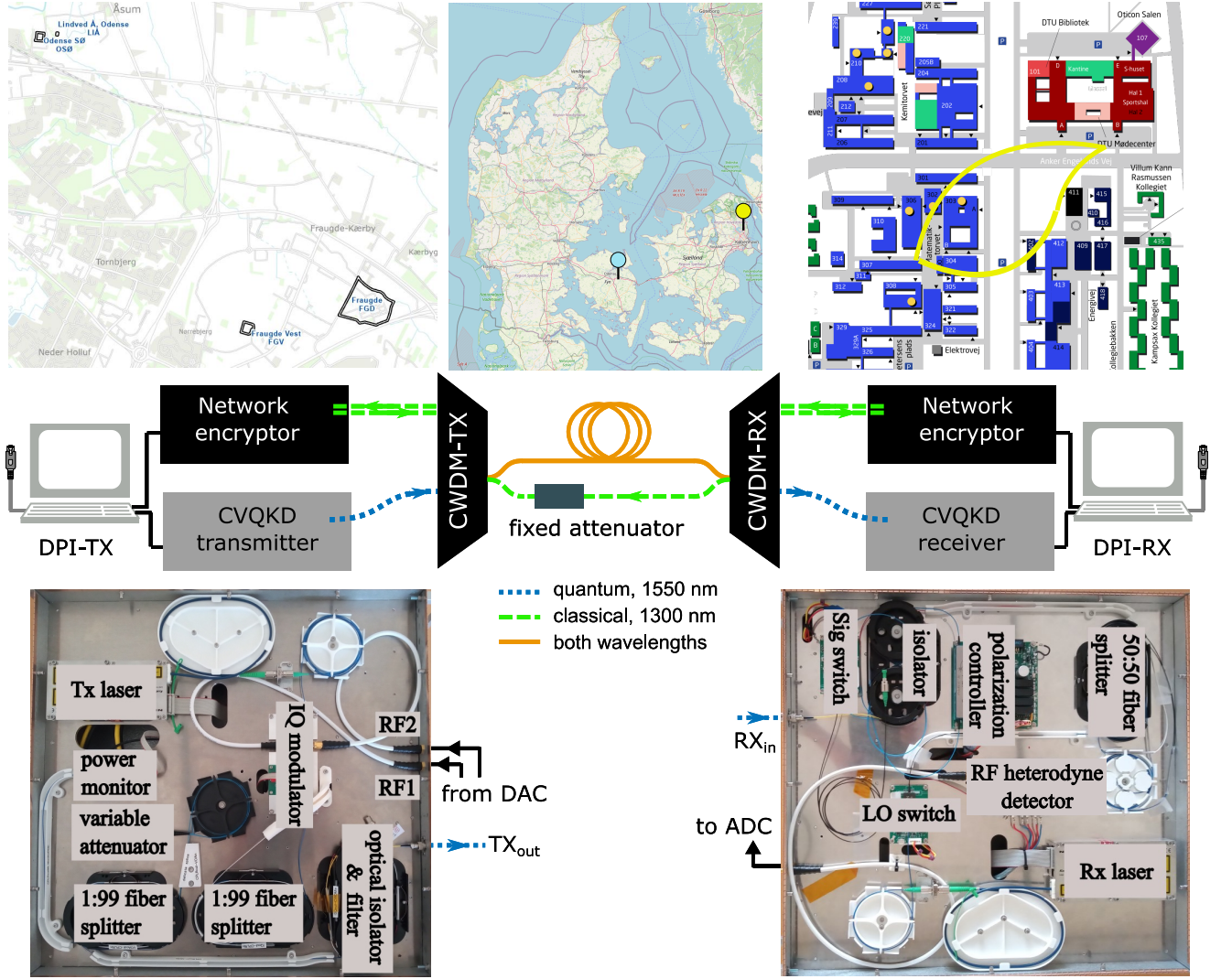


FIG. 1. Practical network encryption with continuous-variable quantum key distribution. (Top) Map of Denmark in the center, with the geographical locations for the experiments indicated using the cyan and yellow pins. On the left is a satellite view showing the power substation locations in Odense, and on the right is a zoomed-in map of DTU. (Bottom) Optical connections are depicted using dashed-green, dotted-blue or solid-orange lines depending on the wavelength(s) of light traversing through them, with a single/pair of line(s) indicating simplex/duplex. A fixed attenuator and a pair of patchcords provide a path for signals at  $\sim 1300$  nm to traverse from RX to TX. The CVQKD-TX and RX modules comprise a solid plate with the optical/optoelectronic components on one side (as shown) and the necessary control electronics on the other. The layer 2 encryptors utilize the AES encryption algorithm with 256 bit long keys. The main text contains a detailed description of all relevant devices as well as the system operation. DPI: digital processing interface.

wires (OPGWs) running between power substations located at Fraugde and South East Odense (Odense SØ), as indicated in the top-left map in Fig. 1. More specifically, two of the links (L2 and L4) were a  $2\times$  and  $4\times$  back-and-forth loop of these aerial fibers, while L3 was a combination of an OPGW and an underground SMF.

Table I summarizes the link lengths, losses (at 1550 nm), and the final results—secret key fractions (SKFs) obtained in the asymptotic limit—for these links. Assuming real-time signal and data processing at the operating rate ( $B = 20$  Mbaud) of our CVQKD system, multiplying the SKF by  $20 \times 10^6$  yields the achievable se-

cret key rate (SKR). With this assumption, the number of AES 256-bit secret key pairs for any of the investigated links far exceeds the key-pair refresh rate requirement of 30 per hour for continuous and real-time operation of the network encryptors.

The CVQKD transmitter (CVQKD-TX) and receiver (CVQKD-RX) are standard 3U 19-inch modules suitable for telecom rack installation. This CVQKD system, coined **qTReX** [17], uses randomness from a state-of-the-art quantum random number generator (QRNG) [18] and a host of digital signal processing (DSP) methods [13, 15, 19] to enable the sharing of quantum correla-

Link label	Location	Length, km	Physical loss, dB	SKF, bits/symbol
L1	Lyngby	0.55	5.5	$0.06 \pm 0.02$
L2	Odense	13.2	4.1	$0.11 \pm 0.02$
L3	Odense	15.3	6.7	$0.05 \pm 0.02$
L4	Odense	25.9	8.9	$0.01 \pm 0.01$

TABLE I. Information about the links investigated and the secret key fraction (SKF) obtained thereon. All 4 links were loopbacks in the sense that both the input and output fiber were physically accessible at the same place. The loss and length at Lyngby were estimated using simple optical power and pulse delay measurements. At Odense, these quantities were determined using an optical time domain reflectometer.

tions between Alice and Bob. Classical information processing steps, applied offline on sequences of data frames from the CVQKD-TX and -RX, utilize these correlations to distill secret keys for the encryptors. The balanced coherent detection employed in CVQKD-RX, together with the large wavelength separation (1550 nm vs 1300 nm) of the quantum and classical signals, ensures that despite being more than 7 orders of magnitude higher in launch power, the classical signal does not have any observable influence on the quantum signal noise characteristics observed at CVQKD-RX.

Currently, the entire setup can operate on the physical layer with minimal user intervention. Once the classical data processing stack is also brought online, the entire operation from quantum states’ production to live data encryption would become fully autonomous. With a few hardware modifications, the qTReX system can be adopted in data-center-like environments [20]. Our work thus serves as a proof-of-concept demonstration of using QKD to ‘future proof’ network encryption technology. We note that QKD has been previously used in a deployed electric utility fiber network for secure authentication of smart grid communications [21].

The paper is organized as follows: In the next section, we provide details of the complete quantum-classical setup that enables future proofing network encryption with CVQKD. This is followed by a description of the conducted experiments and the obtained results. In particular, we describe a novel aspect of the implementation, namely the live optimization of the state of polarization (SOP) of the 1550 nm signal, which is crucial for obtaining a good performance during the quantum phase of the QKD protocol. Finally, we discuss some of the results and provide an outlook before concluding the paper.

## II. SCHEME: CHANNELS & DEVICES

In this section, we present the building blocks of the scheme illustrated in the center of Fig. 1. More specifically, we elaborate on the different communication channels, the connected devices, and their roles in the different stages of the protocol. For an introduction to the princi-

ples of CVQKD as well as typical CVQKD schemes, we refer the reader to reviews in Refs. [6, 22–24].

### A. Quantum channel

The qTReX system uses the so-called sideband coding approach [25] for the preparation and measurement of the quantum states: Information containing complex symbols, with both the real and imaginary parts being a Gaussian random variable, was encoded into and decoded from coherent states, respectively [13, 14].

However, the quantum-optical signal coded at the sideband frequencies is relatively dim. To address the tasks of carrier and clock recovery—necessary for phase-reference alignment and synchronization of the RX and TX—the CVQKD system utilized some ancillary signals with higher signal to noise ratio (SNR). These signals are described later in this section. In contrast to a typical lab-based setup that often uses electronic signals for triggering and reference-clock-sharing between the RX and TX, here, the sole signal path was a one-way optical connection. This is the quantum channel: the thick orange line and the dotted blue lines joined together using the CWDMs in Fig. 1, with optical waveforms labelled  $TX_{\text{out}}$  and  $RX_{\text{in}}$  (bottom of the figure) further visualizing the entry and exit points of this channel.

### B. Classical channel

While the CVQKD devices were connected solely through the quantum channel, their respective digital processing interfaces (DPIs) were connected ‘classically’. Specifically, a pair of workstations on the local network formed a classical channel (not shown in Fig. 1) for the exchange of data between TX and RX during the classical phase of the QKD protocol. Ideally, this classical channel should be authenticated [6], typically achieved using a part of the secret key from an earlier round of the protocol. However, to simplify the overall scheme, we did not implement such authentication.

### C. Encryption channel

For high-speed network encryption (in the 1-100 Gbps range) over dedicated point-to-point links serving data centers, cloud service providers, and large enterprises, fiber-optic small form factor pluggables (SFPs) are the standard solution for distances spanning several kilometers [26].

We used off-the-shelf 100G QSFP28 4WDM-40 hot-pluggable modules [27] for transmitting and receiving the encrypted data. As depicted by the dashed-green line pairs in Fig. 1, these transceiver modules operate in duplex mode. To ensure bidirectional traffic at  $1300 \pm 10$  nm without saturating the SFP receiver at the encryptor

on the TX side, we inserted a fixed attenuator (loss  $\sim 5$  dB at 1300 nm) between the CWDMs. The encryption paths thus constituted the quantum channel and fiber patch cords with the fixed attenuator (TX to RX: solid-orange line, RX to TX: dashed-green line).

#### D. CVQKD-TX

The output of a 1550 nm continuous-wave laser (Tx laser) was fed to an in-phase and quadrature (IQ) modulator, biased for performing carrier suppression and single sideband modulation [28], with the radio frequency (RF) input through ports RF1 and RF2. The RF waveforms were generated using an external digital-to-analog converter (DAC).

The flowchart in Fig. 2(a) illustrates the DSP recipe for creating the digital input to the DAC, while the spectrum of the complex waveform, whose real (imaginary) part is related to RF1 (RF2), is depicted in Fig. 2(b). Uniformly distributed random numbers from the QRNG were transformed into discrete Gaussian-distributed numbers with 6 bits of resolution and a range of 7 standard deviations [18]. To this quantum data, a constant amplitude zero auto correlation sequence was multiplexed in time, while a quadrature phase shift keying (QPSK) data sequence containing a known header and frame identification (ID) information was multiplexed in frequency [15]. The subsequent step of pulse shaping was performed by upsampling to the DAC sampling rate of 1 GSamples/s and applying root raise cosine filtering [13, 14]. After single sideband modulation of the two 20 MHz wide sidebands at 80 and 160 MHz, two pilot tones at 25 MHz and 120 MHz were also multiplexed in frequency as depicted in Fig. 2(b).

Referring to Fig. 1 (bottom), the optical power at the output of the IQ modulator was monitored using a 1:99 fiber splitter and power meter. We could independently set the 1) modulation strength associated with the quantum states, 2) power of the pilot tones, and 3) power in the QPSK data band to desired levels through a combined digital control of signal amplitudes during the DSP procedure, tuning of the voltage output levels of the DAC, and the optical attenuation using an electronically controlled variable attenuator after the IQ modulator.

All fiber-optic components featured polarization maintaining fiber (PMF) pigtails, except the SMF-connectorized wavelength filter and isolator (added to prevent Trojan-horse attacks [29, 30]). The signal  $\text{TX}_{\text{out}}$  was fed by a simplex cable to the input of CWDM-TX.

#### E. CVQKD-RX

The RX laser (same model as the TX laser, but detuned in frequency by around 215 MHz) supplied the local local oscillator (LLO) for coherent heterodyning in a

balanced detector configuration. An external analog-to-digital converter (ADC) sampled the analog output of the detector at 1 GSamples/s. Remotely controlled optical (Sig and LO) switches enabled the acquisition of the IQ modulated signal coming from the quantum channel as well as calibration of the vacuum/shot noise normalization. The high extinction of over 60 dB in these switches ensured that the detector response with a switch in the OFF state is akin to physically disconnecting that fiber.

The red trace in Fig. 2(c) illustrates the modulated signal spectrum measured at the input of the quantum channel. It features the same multiplexed components presented in Fig. 2(b). The spurious features on the right hand side of the beat signal were due to the finite sideband suppression [28]. With the signal beam switch in the OFF state, the ADC captured two signals featuring a variance proportional to vacuum noise plus electronic noise power (with LO switch ON) and only electronic noise power (LO switch OFF). The dotted-blue and dashed-green traces in Fig. 2(c) show the corresponding spectra. Subtracting the two variances yields the normalization factor corresponding to the fundamental vacuum noise.

Due to arbitrary polarization fluctuations in the channel, the incoming signal  $\text{RX}_{\text{in}}$  required polarization control; section III A describes the details of this procedure. The signal polarization is in a desired state when it aligns with the polarization of the LLO, where after, the ADC captured the modulated signal.

The remotely controlled switches and the dynamic polarization controller facilitated frequent and independent vacuum noise calibration and maximising the SNR of the quantum signal, respectively, thus playing a crucial role in the fast and autonomous quantum state measurement.

#### F. Digital Processing Interface

Two workstations formed the DPIs for operating the entire QKD protocol. PCI Express based DAC and ADC cards, housed in these workstations, were used for driving the modulator in CVQKD-TX and acquiring the detector output in CVQKD-RX, respectively, as explained above. The DSP cycles running on each of them allowed the quantum symbols encoded at CVQKD-TX to be eventually decoded at CVQKD-RX, i.e., fulfil the state preparation and measurement tasks. Figure 3 in Ref. [15] shows a flowchart of the DSP running on CVQKD-RX, complementary to the one Fig. 2(a).

Thereafter, graphic processing unit (GPU) equipped workstations communicated over the classical channel to perform the remaining data processing stages of the protocol, namely information reconciliation (IR), parameter estimation (PE), and privacy amplification (PA). Usage of GPU speeds up the execution of both IR and PA.

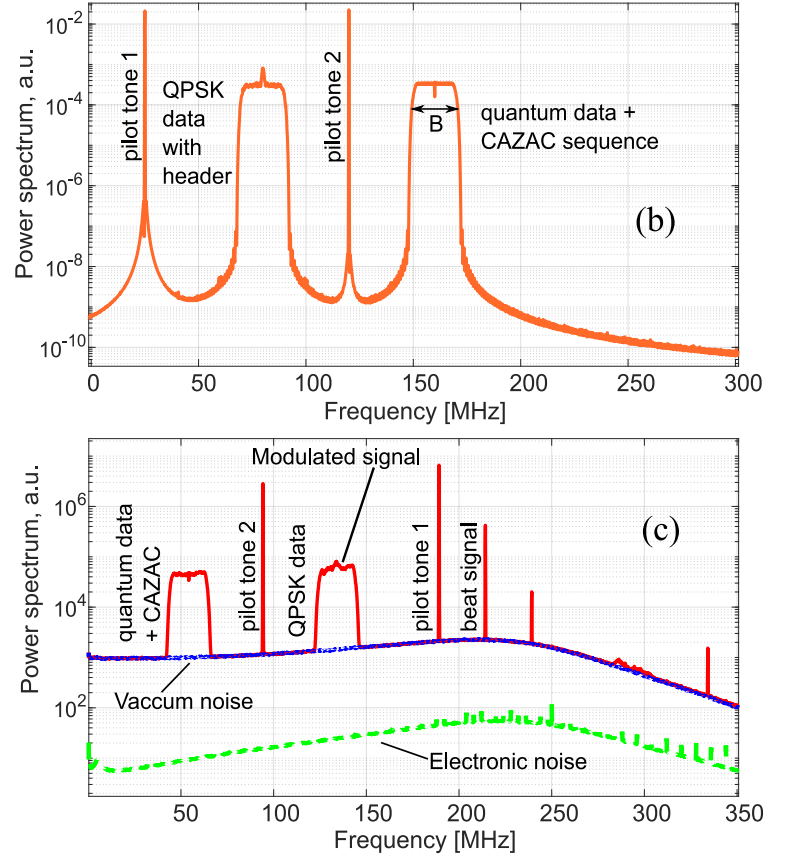
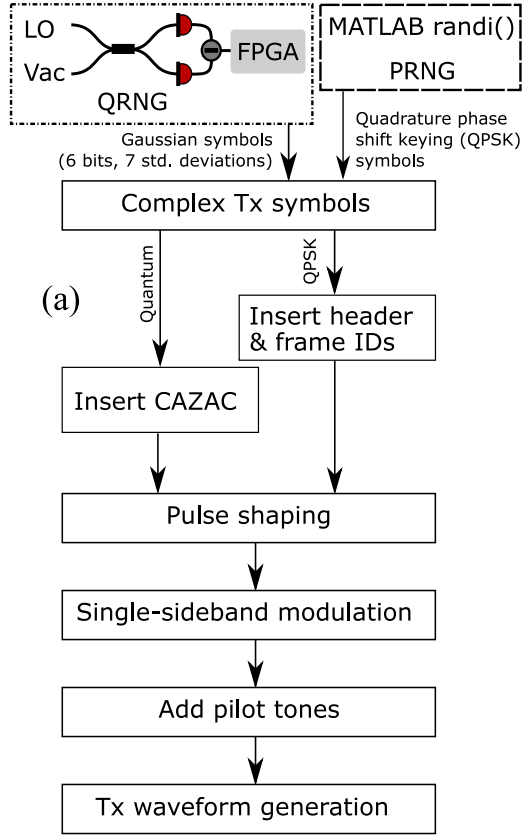


FIG. 2. Digital signal processing (DSP) in **qTReX**. (a) Flowchart showing the various DSP steps for encoding of the quantum states in a  $B = 20$  MHz wide sideband together with several time- and frequency-multiplexed ancillary signals. (b) Spectrum of the complex signal, the real and imaginary parts of which are played out using the two channels of the DAC. (c) Spectra of the ADC captured signals under various configurations of the optical switches in CVQKD-RX, detailed further in the text. Vac: quantum vacuum state  $|0\rangle$ , LO: local oscillator, Q/PRNG: quantum/pseudo random number generator. CAZAC: constant amplitude zero auto correlation.

### G. Network encryptors

Commercially available network encryptors from Zybersafe [16] that support the 100G Ethernet line interface and implement AES in the 256-Galois counter mode were used. The encryptors support a LAN and WAN interface for transport of the unencrypted and encrypted data, respectively. The keys were refreshed every 2 minutes or after a maximum of  $2^{32}$  message frames, with the frame size being 864 bits.

The secret key material generated at the end of the QKD protocol was offloaded to a file, and a simple key management server running on each workstation loaded the content of these files into the encryptor using a serial connection. A pair of AES 256-bit keys (512 bits in total) at a time were supplied to the respective Ethernet encryptor for both encryption and decryption of the messages. Key IDs for these pairs were sequentially generated and exchanged on the encryption channel to verify that both encryptors used the correct key.

## III. IMPLEMENTATION & RESULTS

The goal of any QKD protocol implementation is to maximize the SKF under the given channel conditions. Before delving into the general details of the protocol runs, we first describe our efforts to overcome the challenge of polarization optimization, which plays a crucial role in the long-term and autonomous operation of **qTReX** as well as in maximisation of the SKF.

### A. Dynamic polarization optimization

We optimized the polarization of the incoming optical signal using the so-called simultaneous perturbation stochastic approximation (SPSA) method [31]. We used a commercial polarization controller integrated with four piezoelectric actuators with an off-the-shelf 16-bit multi-channel DAC supplying the input voltages to the drivers of the actuators.

Controlling the SOP of the modulated signal so that it matches with the SOP of the LLO yields a stronger RF

heterodyne output. The objective function to maximize was the overall power  $R$  of the RF heterodyne signal, the spectrum of which is shown in Fig. 2(c) by the red trace (with the background noise contribution shown by the blue trace). We remark here that even after channel attenuation, the SNR was reasonably large, simply due to the various multiplexed ancillary signals. And finally, also note that the SOP of the LLO was fixed by virtue of using only PMF components, namely the Rx laser, LO switch, and 50:50 fiber splitter; see Fig. 1.

The optimization was executed in a feedback loop, iteratively seeking to increase the power  $R_n$  and settle around a maximum after some  $n = N$  rounds; typically  $N \leq 35$  sufficed for our system. At the end of iteration  $n$ , ‘optimized’ digital inputs  $\vec{v}_{n+1}$  for the multi-channel DAC were evaluated using digital inputs  $\vec{v}_n$  and a gradient estimate  $\vec{g}_n$  as  $\vec{v}_{n+1} = \vec{v}_n - b_n \vec{g}_n$ . Here,  $b_n$  denotes a pre-calculated scalar gain coefficient, and the vector sign is to convey that the operation was on 4 channels simultaneously. The calculation of  $\vec{g}_n$  during the iteration involved applying successive positive and negative perturbations  $\vec{v}_n + p_n \vec{d}_n$  and  $\vec{v}_n - p_n \vec{d}_n$ , respectively, and measuring the corresponding powers  $R_n^+$  and  $R_n^-$  to yield

$$\vec{g}_n = \left( \frac{R_n^- - R_n^+}{2p_n} \right) \vec{d}_n. \quad (1)$$

In the above,  $p_n$  denotes a pre-calculated scalar perturbation coefficient, while  $\vec{d}_n$  is a vector with elements 1 or  $-1$  drawn from a Bernoulli distribution, with both elements being equally likely.

Table II shows the log from a typical run of the polarization optimization task. The four columns in the center are the components of  $\vec{v}_n$ , while the corresponding evolution of powers  $R_n$  is presented in the last column. One can observe that  $R_n$  initially goes down but quickly recovers and settles to a maximum after  $n \sim 20$ . The corresponding size of the perturbation kicks ( $|\vec{v}_{n+1} - \vec{v}_n|$ ) follows the same behaviour. Note that at the beginning of the optimization task, we measure the background noise power  $R_0$  (due to vacuum + electronic noise) by making use of the Sig switch, and subtract it from the total power in the RF heterodyne measurement.

The stochastic nature of SPSA is embedded in the fact that  $\vec{d}_n$  is chosen randomly in every iteration. The choice of scalars  $b_n$  and  $p_n$  is critical to the performance of SPSA [31]. Through empirical tests on L1, i.e., the campus loop at DTU (see Table I), we found that  $p_n = p_0 n^{-0.5}$  and  $b_n = b_0 n^{-0.75}$  with  $p_0$  and  $b_0$  in the neighbourhood of 350 and 200000, respectively, yielded a relatively fast and stable convergence, such as the one shown in Table II. We note that there can be other combinations  $p_0$  and  $b_0$  that can yield a similar performance.

On links L2-L4, we faced more challenges in determining appropriate  $p_n$  and  $b_n$  due to which the eventual performance of the algorithm was somewhat worse. This was however not unexpected as compared to underground fibers, the rate of change of the SOP of a lightwave in OPGWs can be much higher, as they are exposed to not

TABLE II. Polarization optimization task log from one of several experiments performed at DTU Lyngby. The components of the vector  $\vec{v}_n$  in columns 2-5 are the digital inputs of four 16-bit DACs. A background noise power  $R_0 = 33.831$  is already corrected for in the last column. All DACs are initialized in the beginning to  $v_1[j] = 2^{15} - 1 = 32767$ ,  $j \in [1, 4]$ , to have the maximum operating range.

$n$	$v_n[0]$	$v_n[1]$	$v_n[2]$	$v_n[3]$	$R_n$
1	32767	32767	32767	32767	92.863
2	38091	27443	38091	27443	65.792
3	39488	26046	36694	28840	69.726
4	39032	26502	36238	28384	72.070
5	38189	27345	37081	29227	78.407
6	36971	26127	35863	30445	90.376
7	37044	26054	35936	30518	93.489
8	36695	26403	36285	30867	98.593
9	36445	26153	36535	30617	98.523
10	36228	25936	36318	30834	100.421
11	35804	26360	35894	31258	103.931
12	35612	26552	36086	31066	104.661
13	34746	27418	35220	31932	118.385
14	35050	27114	34916	32236	113.494
15	34968	27032	34998	32318	113.732
16	34957	27021	34987	32307	112.943
17	34861	26925	35083	32403	114.292
18	34588	27198	34810	32676	115.751
19	34388	27398	35010	32476	116.653
20	34248	27538	35150	32616	118.133
21	33986	27800	35412	32878	118.465
22	34080	27706	35506	32784	118.291
23	34111	27737	35537	32815	118.177
24	33977	27603	35671	32949	118.283
25	34023	27649	35717	32995	117.585
26	34155	27781	35585	33127	118.492
27	34154	27780	35586	33126	117.902
28	34120	27814	35620	33160	119.007
29	34138	27832	35638	33142	118.035
30	34085	27779	35691	33195	118.137
31	34077	27787	35699	33203	117.726
32	34084	27794	35706	33210	118.448
33	34026	27736	35764	33268	117.808
34	33979	27783	35717	33315	117.717
35	33971	27791	35725	33323	117.888

only larger and faster temperature variations but also the natural forces of wind and lightning [32]. With long-term testing (over few weeks or even months), we expect to be able to characterize these links more properly.

## B. Protocol runs: Quantum phase

State machines running in a loop independently on both CVQKD-TX and CVQKD-RX used the quantum

channel for transmission and reception, respectively, of the information carrying signal at 1550 nm, spectral representations of which are shown in Fig. 2(b) and (by the red trace) in Fig. 2(c). Simultaneously, the network encryptors described in subsection II G were set to operate continuously using secret keys generated from prior runs of the CVQKD system, implying that the quantum channel was also inundated with the 1300 nm signal.

At the RX, the task of polarization optimization, already described in subsection III A, was followed by the ADC capturing samples of the modulated signal, using a level trigger set adaptively on the ADC channel itself that acquires the data. For this, in every round, the TX played out sequentially a total of 1000 frames, each constructed with 0.2M unique Gaussian symbols using the DSP chain shown in Fig. 2(a). This burst from the TX lasted just around 3 mins, after which, it was left in an idle state until the start of the next round, which had a duration of 10 minutes.

While the RX was programmed to capture and store—as a file on disk—a maximum of 100 of these data frames, in practice, the yield was typically less due to timeouts (set-trigger-level too high) or due to capturing of noise between successive TX frames (set-trigger-level too low). After acquiring the data with modulation, a total of  $2 \times 2\text{G}$  ADC samples for performing the task of vacuum noise calibration, described in section II E, were captured. The switches routing the Sig and LO away from the detector for this purpose were then reverted to their original positions, and CVQKD-RX was then also left in an idle state until the next round. The duty cycle at the RX was typically between 70 – 80%.

Once the captured data files from all 6 rounds were available, DSP routines based on a machine learning framework [13] operating at DPI-RX kicked in. Using the various ancillary signals, the digital synchronization procedure was performed. In particular, the pilot tones assisted in clock and carrier recovery, while the QPSK band helped in optimal sampling [13, 15]. The latter relies on the fact that the QPSK data contained a sequence of symbols known to both TX and RX. After extracting some frame IDs, the demodulation of the QPSK band was completed. With all the frequency, phase, and temporal information obtained, the Gaussian quantum symbols could also be optimally extracted.

Figure 3 shows various results from experiments conducted on L2–L4 at Odense. Out of the  $2 \times 10^8$  quantum states generated at the TX every round, Fig. 3(a) shows the number of quantum states that were successfully measured at the RX. Figures 3(b) and (c) show respectively the evolution of the measured SNR of the pilot tone and the main outcome of the vacuum noise calibration procedure described above. At the TX, while the quantum phase of the protocol was  $6 \times 10 = 60$  mins long, at the RX, it took around 3 times longer as the DSP was not performed in real time.

### C. Protocol runs: Classical phase

With the quantum stage of the protocol finished, the classical data processing steps of IR, PE, and PA were also performed offline. The IR was based on a multi-dimensional reverse reconciliation scheme and a bank of multi-edge-type low-density-parity-check codes were used [33]. Due to a limited number of code rates, high-performance IR was actually possible only in some selected rounds, three of which are indicated by the triangle, circle and hexagon shapes around the markers in Fig. 3(g). In these cases, we obtained a reconciliation efficiency  $\beta \approx 95\%$  at a frame error rate (FER) in the vicinity of 0.5. In subsection IV B, we further elaborate on this matter.

Alice performed PE using her filtered symbols and the recovered quantum symbols of Bob, which, together with the variables such as the electronic and vacuum noise variances from various calibrations in RX, were shared by Bob via the authenticated channel. After calculating the covariance matrix, the total noise  $\xi$  and transmittance  $\eta$  were evaluated. These could be partitioned into trusted and untrusted components [14] using the vacuum noise normalization values shown in Fig. 3(c), and the optical transmittance of the receiver (including CWDM-RX)  $\eta_t = 0.33$ . Figures 3(d) and (e) show the untrusted components  $\eta_u = \eta/\eta_t$  of the transmittance (converted to loss in dB) and noise  $\xi_u = \xi - \xi_t$  respectively, from the 6 rounds, while the trusted noise values  $\xi_t$  themselves are shown in Fig. 3(f). As is often done in CVQKD, the noise is conveyed as whatever is in excess of the shot/vacuum noise in a relative sense, i.e., in shot noise unit (SNU). Together, these quantities aid in the calculation of  $\chi_{BE}$ , i.e., Eve’s Holevo information.

The results from PE enable us to estimate the SKR, given by

$$\text{SKR} = B(1 - \text{FER})(\beta I_{AB} - \chi_{BE}). \quad (2)$$

The mutual information  $I_{AB}$  between Alice and Bob is also calculated using the covariance matrix.

Figure 3(g) shows the SKR values for the experiments performed on L2–L4 at Odense. We emphasize that such rates can be achieved in practice under the assumptions (justified below in Section IV) that (1) the DSP, IR, and PA can be performed in real time, and (2) it is always possible to obtain  $\beta = 95\%$ ,  $\text{FER} \approx 0.5$ . Based on that, the average SKR obtained from the experiments on L1 at Lyngby (not shown in Fig. 3) would be around 1.1 Mbps.

From a security perspective, the generated keys here are secure in the asymptotic regime, and assuming collective attacks by Eve [22, 34]. We remark that a composable key analysis [14] would likely not have yielded any positive SKR due to the not-too-large number of quantum states obtained in the experiments here as well as the relatively worse trusted loss ( $\eta_t = 0.33$  for qTReX versus  $\eta_t = 0.68$  in Ref. [14]).

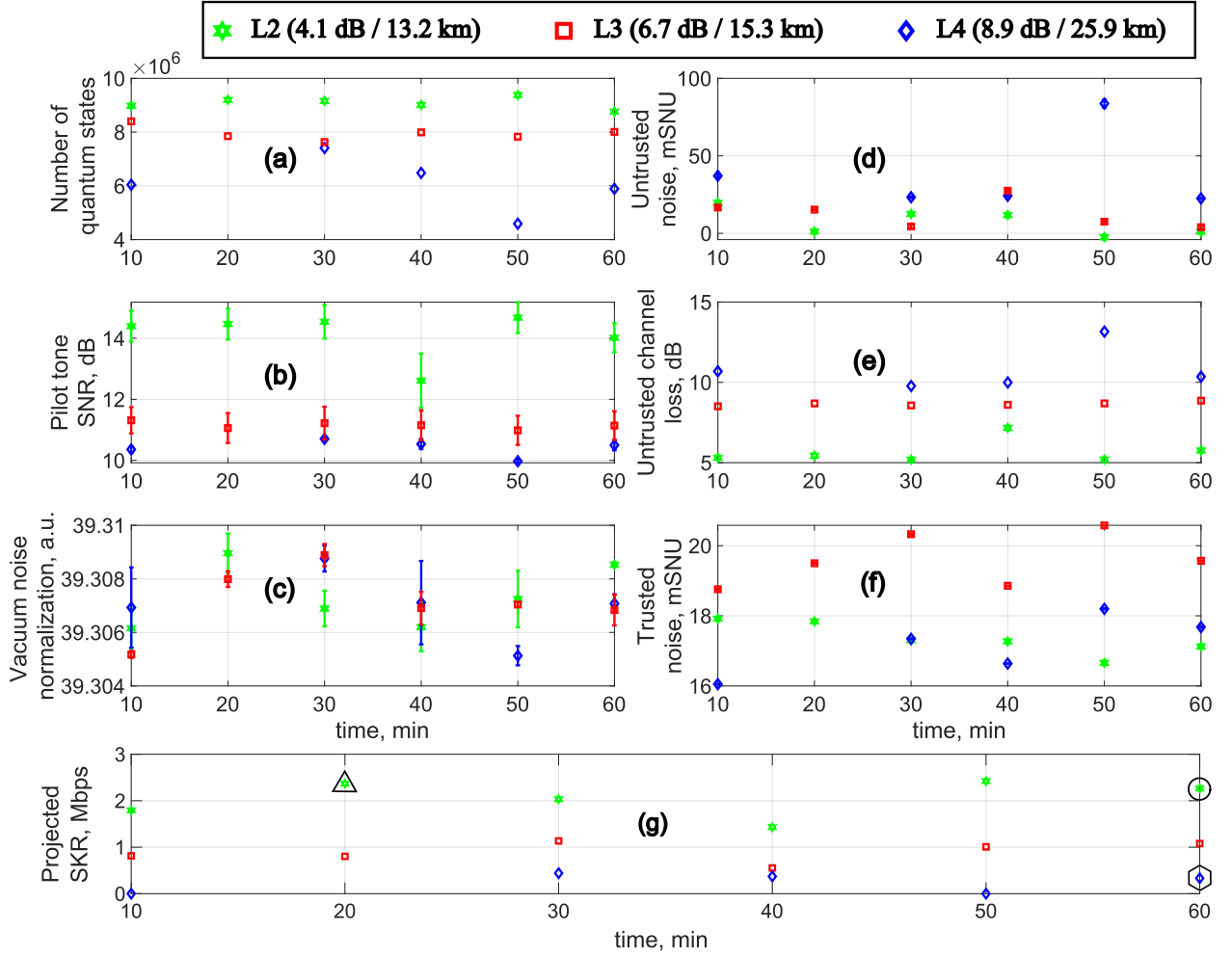


FIG. 3. (Color online) Various results from the parameter estimation and calibration procedures in the tests carried out at the 3 links in Odense (refer Table I for more info). (a) Number of quantum states that were successfully prepared by TX as well as measured by RX. (b) Strength of the pilot tone which aids in the clock and carrier recovery. (c) Outcome of the calibration procedure performed after every round of modulation and acquisition. (d) and (e) Noise and loss attributed to Eve. (f) Noise assumed to be beyond Eve’s control. (g) Projected secret key rate (SKR) assuming the DSP and information reconciliation had been performed in real time. A reconciliation efficiency  $\beta = 95\%$  and FER = 0.5 was uniformly assumed in the calculations, and in the 3 cases marked by a hexagon, circle, and a triangle, it was actually also achieved (further details in the main text). Also, in all the non-marked cases, PE was performed using all the symbols of Alice and Bob.

#### IV. DISCUSSION

In this section, we discuss some aspects of our implementation as well as the obtained results in more detail.

##### A. Loss: Untrusted vs Physical

The channel loss values graphed in Fig. 3(e) over the 6 rounds show a considerable fluctuation, especially for OPGW $\times 2$  and OPGW $\times 4$ , or links L2 and L4, respectively. Furthermore, comparing with the physical loss values presented in Table I, a difference of at least 0.8 dB is evident. The latter can partly be explained due to the fixed loss coming from two extra fiber adapters that

were used for connecting to the loopbacks in L2-L4; since they were absent during the OTDR measurements, their combined loss is not included in the entries of Table I.

The fluctuation on the other hand stems from the subpar performance of the SOP optimization in case of OPGWs, which was explained at the end of subsection III A. A poor SOP reduces the mode-matching efficiency of the LLO with the optical signal (containing both the quantum data and the ancillary signals; see subsection II E) entering CVQKD-RX, which can make the execution of the overall DSP chain at RX inefficient as well [15]. To elaborate, the SNR of the pilot tone plays an important role in ensuring a proper functioning of the machine learning framework, and when this SNR goes down, the performance of the carrier and clock recovery also worsens, causing the PE evaluated noise and/or

loss to rise. This can be observed through the correlated trend shown by the green/blue markers for L2/L4 in Figs. 3(b) and 3(e). In the worst case, the machine learning framework can even completely fail during the state measurement and no symbols can be decoded; this was for instance the outcome in round 2 for link L4.

While the SOP optimization parameters can be chosen more carefully after a longer and more thorough characterization of the aerial fibers, another alternative is to use a so-called polarization hybrid [35, 36].

## B. Practical and real-time data processing

As presented in the previous section, the bottlenecks in the implementation of the CVQKD protocol stack primarily come from the DSP at RX as well as the IR and PA procedures. Also, for a fully autonomous operation, the data processing pipelines at both TX and RX require synchronization.

We are currently working on some major revisions in our DSP software chain and in the near future, also plan to port the DSP routines on an FPGA where we expect a considerable speedup. Furthermore, we already have an IR framework capable of performing multidimensional reconciliation as well as privacy amplification in near real time. To elaborate, on an Intel Core i7-9750H CPU (with 6 cores and 2.60 GHz as the processor base frequency) and an NVIDIA GeForce RTX 2060 Mobile GPU (with 1920 cores and 6 GB memory), the IR and PA throughput can reach 9.85 MBaud, which is almost half of the raw symbol rate. All in all, we believe with all these advances, it will be possible to achieve the data processing pipeline for the CVQKD protocol to operate close to  $B = 20$  MBaud in the near future.

The main challenge that then remains to solve is how to pick the appropriate input parameters such as the code rate, the log likelihood ratio factor, etc. that ensure a single-shot reconciliation with the simultaneous assurance of a high  $\beta$  at a reasonable FER. The overall IR performance is fairly sensitive to the choice of these parameters, which also need to be frequently adjusted in case of channels with a fluctuating transmittance. For this, we are currently working on an algorithm that uses the ancillary signals to enable a dynamic calculation of these input parameters which can then make the IR part

of the classical data processing stack meet all the aforementioned requirements. This would allow developing a feedback between TX and RX to optimize the modulation strength, thus maximising the SKR for the given channel parameters.

## V. CONCLUSION & OUTLOOK

In conclusion, we have reported the field deployment of a semi-autonomous continuous variable quantum key distribution (CVQKD) system that powers a network encryption scheme to establish quantum-secure data transfer links at two locations in Denmark. More specifically, system operation in a power substation (critical infrastructure) environment and the ability to perform quantum communication over different types of channels that are a combination of underground and aerial fibers is showcased. The CVQKD system operates at 1550 nm while the network encryptors operate at 1300 nm and use the same (wavelength-multiplexed) channel for the transport of both quantum states as well as encrypted data. Despite the several orders of magnitude difference in optical powers, the scheme is able to have a positive secret key yield, exhibiting another successful quantum-classical integration example. Such a crypto-agile platform can be used to future proof the security of network data infrastructure, such as data center interconnections.

## VI. ACKNOWLEDGEMENTS

We would like to thank Danish e-infrastructure Co-operation (DeiC) for the equipment loan as well as the use of the loopback fiber at DTU. We are also thankful to Morten Houborg Andersen, Alexander Frederiksen, and Thomas Wisbech from Energinet for valuable discussions as well as facilitating the equipment installation at the substation in Fraugde. We acknowledge support from Innovation Fund Denmark (CryptQ project, grant agreement no. 0175-00018A) and the Danish National Research Foundation, Center for Macroscopic Quantum States (bigQ, DNRF142). This project has received funding from the European Union's Digital Europe programme under Grant agreement No 101091659 (QCI.DK).

- 
- [1] J. M. Porup, "How a nuclear plant got hacked," <https://www.csoonline.com/article/568145/how-a-nuclear-plant-got-hacked.html>. Accessed: 2023-11-23.
  - [2] "The Colonial Pipeline Hack Is a New Extreme for Ransomware," <https://www.wired.com/story/colonial-pipeline-ransomware-attack/>. Accessed: 2023-11-23.
  - [3] "The attack against Danish, critical infrastructure," [https://sektorcert.dk/wp-content/uploads/](https://sektorcert.dk/wp-content/uploads/2023/11/SektorCERT-The-attack-against-Danish-critical-infrastructure-TLP-CLEAR.pdf)

- [2023/11/SektorCERT-The-attack-against-Danish-critical-infrastructure-TLP-CLEAR.pdf](https://sektorcert.dk/wp-content/uploads/2023/11/SektorCERT-The-attack-against-Danish-critical-infrastructure-TLP-CLEAR.pdf). Accessed: 2023-11-25.
- [4] IEEE Std 802.1AE-2018 (Revision of IEEE Std 802.1AE-2006) pp. 1–239 (2018).
- [5] C. H. Bennett and G. Brassard, Theoretical Computer Science **560**, 7–11 (2014). Theoretical Aspects of Quantum Cryptography – celebrating 30 years of BB84.

- [6] V. Scarani, H. Bechmann-Pasquinucci *et al.*, Reviews of Modern Physics **81**, 1301–1350 (2009).
- [7] S. Pirandola, Physical Review Research **3**, 013279 (2021).
- [8] I. Choi, Y. R. Zhou *et al.*, Optics Express **22**, 23121–23128 (2014). Publisher: Optica Publishing Group.
- [9] T. A. Eriksson, T. Hirano *et al.*, Communications Physics **2**, 9 (2019).
- [10] R. I. Woodward, J. F. Dynes *et al.*, “Quantum Key Secured Communications Field Trial for Industry 4.0,” in “2021 Optical Fiber Communications Conference and Exhibition (OFC),” (2021), pp. 1–3.
- [11] B.-X. Wang, S.-B. Tang *et al.*, Opt. Express **29**, 38582–38590 (2021).
- [12] H. H. Brunner, C.-H. F. Fung *et al.*, EPJ Quantum Technology **10**, 1–12 (2023). Number: 1 Publisher: SpringerOpen.
- [13] H.-M. Chin, N. Jain *et al.*, npj Quantum Information **7**, 20 (2021).
- [14] N. Jain, H.-M. Chin *et al.*, Nature Communications **13**, 4740 (2022).
- [15] H.-M. Chin, N. Jain *et al.*, Quantum Science and Technology **7**, 045006 (2022).
- [16] “Zybersafe TrafficCloak – Datasheet,” <https://zybersafe.com/wordpress/wp-content/uploads/2019/11/Zybersafe-Data-Sheet.pdf>. Accessed: 2023-01-03.
- [17] N. Jain, H.-M. Chin *et al.*, “qTReX : A semi-autonomous continuous-variable quantum key distribution system,” More information at <https://www.ofcconference.org/en-us/home/eposters/poster/?id=3689698>.
- [18] T. Gehring, C. Lupo *et al.*, Nature Communications **12**, 1–11 (2021).
- [19] S. Kleis, M. Rueckmann, and C. G. Schaeffer, Optics Letters **42**, 1588–1591 (2017).
- [20] “Using QKD for Data Center Security,” <https://www.copenhagenfintech.dk/projects/using-qkd-for-data-center-security>. Accessed: 2023-12-10.
- [21] M. Alshowkan, P. G. Evans *et al.*, Scientific Reports **12**, 12731 (2022). Number: 1 Publisher: Nature Publishing Group.
- [22] E. Diamanti and A. Leverrier, Entropy **17**, 6072–6092 (2015).
- [23] F. Laudenbach, C. Pacher *et al.*, Advanced Quantum Technologies **1**, 1800011 (2018).
- [24] S. Pirandola, U. L. Andersen *et al.*, Advances in Optics and Photonics **12**, 1012 (2020).
- [25] A. M. Lance, T. Symul *et al.*, Physical Review Letters **95**, 180503 (2005).
- [26] “A move to high speed server connectivity in the cloud,” <https://www.cisco.com/c/en/us/products/collateral/interfaces-modules/transceiver-modules/high-speed-server-con-cloud-wp.html>. Accessed: 2023-11-03.
- [27] “QSFP28 100G 4WDM-40 transceiver,” <https://apps.juniper.net/hct/model/?component=QSFP-100G-4WDM40>. Accessed: 2023-11-03.
- [28] N. Jain, I. Derkach *et al.*, Quantum Science and Technology **6** (2021).
- [29] N. Gisin, S. Fasel *et al.*, Physical Review A **73**, 022320 (2006). ArXiv: quant-ph/0507063.
- [30] N. Jain, B. Stiller *et al.*, IEEE Journal on Selected Topic in Quatum Electronics **21**, 1077–260X (2014).
- [31] J. Spall, IEEE Transactions on Automatic Control **37**, 332–341 (1992).
- [32] D. Charlton, S. Clarke *et al.*, Opt. Express **25**, 9689–9696 (2017).
- [33] H. Mani, T. Gehring *et al.*, Phys. Rev. A **103**, 062419 (2021).
- [34] F. Grosshans, G. Van Assche *et al.*, Nature **421**, 238–241 (2003).
- [35] D. Pereira, A. N. Pinto, and N. A. Silva, Journal of Light-wave Technology **41**, 432–439 (2023).
- [36] H.-M. Chin, A. A. Hajomer *et al.*, “Machine learning based joint polarization and phase compensation for cv-qkd,” in “2023 Optical Fiber Communications Conference and Exhibition (OFC),” (2023), pp. 1–3.